CRYSTAL GROWTH & DESIGN

pubs.acs.org/crystal

Article

Effect of Titanium Induced Chemical Inhomogeneity on Crystal Structure, Electronic Structure, and Optical Properties of Wide Band Gap Ga_2O_3

Mallesham Bandi,*,▽ Vishal Zade,▽ Swadipta Roy, Aruna N. Nair, Sierra Seacat, Sreeprasad Sreenivasan, V. Shutthanandan, Chris G. Van de Walle, Hartwin Peelaers, and C. V. Ramana*

Cite This: *Cryst. Growth Des.* 2020, 20, 1422−1433

Read Online

ACCESS | Metrics & More | Article Recommendations

ABSTRACT: Tailoring the optical and electronic properties of wide band gap β-Ga_2O_3 has been of tremendous importance to utilize the full potential of the material in current and emerging technological applications in electronics, optics, and optoelectronics. In the present work, we report the effect of Ti-dopant insolubility driven chemical inhomogeneity on the structural, morphological, chemical bonding, electronic structure, and band gap red shift characteristics in Ga_2O_3 polycrystalline compounds. $Ga_{2-2x}Ti_xO_3$ (GTO; $0 \le x \le 0.20$) compounds were synthesized using a conventional high-temperature solid state reaction route under variable calcination temperatures (1050−1250 °C) while sintering was performed at 1350 °C. X-ray diffraction analysis of GTO samples reveals that the formation of single-phase compounds occurs only at a very low concentration of Ti doping (<5 at. %), whereas higher Ti doping results in composite formation with a significant undissolved TiO_2 rutile phase. However, in sintered samples, fraction of undissolved rutile phase transformed into monoclinic TiO_2. Rietveld refinement of intrinsic Ga_2O_3 and single-phase Ti-doped compound ($x = 0.05$) confirms that samples are stabilized in monoclinic symmetry with $C2/m$ space group. Surface morphologies of samples reveal that intrinsic Ga_2O_3 exhibits rod shaped morphology, while Ti-doped compounds exhibit spherical morphology. Moreover, in doped compounds with abnormal grain growth, lattice twinning induced striations were noted in contrast to intrinsic Ga_2O_3. High-resolution X-ray photoelectron spectroscopic analysis of Ga 2p shows a positive shift compared to metallic Ga due to interaction between the electron cloud of adjacent ions. Ti $2p_{1/2}$ spectra show anomalous broadening due to the Coster−Kronig effect. First-principles calculations using hybrid density functional theory show that Ti preferentially substitutes on octahedral Ga sites and that it behaves as a deep donor in Ga_2O_3. From the optical absorption spectra, a red shift in the optical band gap is observed. Absorption within the band gap of Ga_2O_3 is attributed to the inclusion of undissolved TiO_2, as TiO_2 has a type I alignment within the gap of Ga_2O_3. In addition, the electrocatalytic behavior of GTO compounds was examined. From electrocatalytic studies it is evident that doped compounds exhibit appreciable electrocatalytic activity in contrast to intrinsic Ga_2O_3.

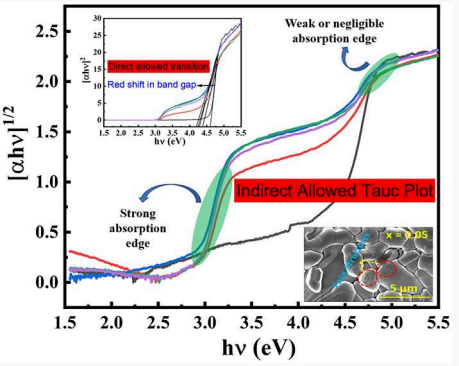

1. INTRODUCTION

β-Ga_2O_3 is an important and extensively studied wide band gap semiconductor due to its numerous applications ranging from semiconducting lasers,[1] field effect devices,[2] flat panel devices,[3] photoluminescence,[4] high-temperature gas sensors,[5] photocatalyst,[6,7] deep-UV photodetector,[8−10] and transparent conducting electrode (TCO).[11,12] β-Ga_2O_3 exhibits good thermal and chemical stability as compared to other polymorphs, which are thermodynamically unstable, and converts to β-Ga_2O_3 upon heat treatment.[13] The mainstream of Ga_2O_3 research is on the periphery even though it has been known for decades; however, for the past decade the research has intensified as a prospective wide band gap material in terms of science and technology and an alternative to SiC and GaN for ultrahigh-voltage power devices.[13,14] In recent years, the interest in electronic and optical properties of β-Ga_2O_3 has also increased to exploit in wide range of gas sensing and optoelectronic device applications.[15]

β-Ga_2O_3 is stabilized in monoclinic crystal symmetry with $C2/m$ space group at ambient conditions.[16,17] The typical reported optical band gap values of β-Ga_2O_3 vary in the range 4.4−4.9 eV,[18] and in the range of 300−1000 nm wavelength, it exhibits optical transmittance greater than 80%.[19] β-Ga_2O_3 exhibits high electric breakdown strength and Bagila's figure of merit of 2000−3400, which makes it useful for high-power devices.[20,21] Superior structural and physical properties,

Received: June 11, 2019
Revised: January 22, 2020
Published: January 23, 2020

availability of β-Ga_2O_3 bulk substrates, and the ability to fabricate in thin film form through various techniques, makes it a representative candidate for next generation aforementioned device applications.[22]

However, continuous efforts of researchers by several approaches are underway to solve the fundamental problems associated with the material [p-type conductivity][18,23] and to tailor the properties for realizing new device applications. Doping with metallic and non-metallic elements is one of the efficient approaches in order to achieve desired and controllable properties. There are quite a number of reports on β-Ga_2O_3 that deal with the effect of elemental doping on electronic and optical properties. For instance, β-Ga_2O_3 as a promising wide band gap transparent semiconductor requires a controllable carrier density. The as-grown material is usually unintentionally n-type. This cannot be attributed to oxygen vacancies, which are deep donors with a very large ionization energy.[24] It has been reported that doping with Si and Sn can enhance the free electron carrier concentration beyond 10^{19} cm^{-3}.[22,25−27] The optical properties of β-Ga_2O_3 can be altered depending on the type of dopants (acceptor or donor). The blue shift in optical band gap is reported in Mg (deep acceptor) doped Ga_2O_3 thin films,[28] whereas a red shift in the optical band gap is reported in W, Mo, and Ti (donors) doped thin films.[29−31] In addition to altering the optical band gap, the luminescence properties of β-Ga_2O_3 and other polymorphs of Ga_2O_3 are well-reported in literature. In β-Ga_2O_3 blue luminescence was observed.[32] Moreover, PL properties of colloidal γ-Ga_2O_3 nanocrystals (NCs) were also investigated, showing that these nanocrystals exhibit size tunable PL from ultraviolet to blue.[33] The PL efficiency and dynamics strongly depended on NC size, structure, and surface modification.[34] Eu-doped colloidal γ-Ga_2O_3 nanocrystals with coexisting Eu-dopant oxidation states (Eu^{3+} and Eu^{2+}) exhibit complex photoluminescence (PL) properties.[35] In addition, PL properties of colloidal lanthanide(III)-doped Ga_2O_3 nanocrystals were studied in detail. Eu^{3+}-doped Ga_2O_3 nanocrystals exhibit red and blue emission resulting from intra-4f orbital transitions. Dual blue-green PL emission of Tb^{3+}-doped Ga_2O_3 nanocrystals was also demonstrated.[36]

The optical and electronic properties of β-Ga_2O_3 such as photoluminescence, transmittance, optical band gap, carrier concentration, and chemical bonding are strongly coupled with the solubility of a particular dopant in the parent matrix, chemical inhomogeneity that resulted by doping, and microstructure. The fundamental problem associated with Ga_2O_3 is insolubility of dopants beyond a certain concentration. Hence, solubility and insolubility in doped β-Ga_2O_3 compounds lead to variation in chemical inhomogeneity and microstructure, and as a consequence variation in optical and electronic properties. Most of the studies deal with the effect of doping on optical properties of thin films. But thin film fabrication is a non-equilibrium process, and an optimized conclusion cannot be derived in terms of the fundamental science associated with dopant induced changes in chemical and optical behavior which may be influenced by variation in chemical inhomogeneity and microstructure. To the best of our knowledge, studies focused toward understanding the effect of doing in β-Ga_2O_3 ceramics are scarce. Recently, we reported the effect of W doping into β-Ga_2O_3 on the crystal structure, microstructure, optical band gap, and changes in chemical bonding.[37,38] Similarly, Fe doping on structural and microstructural features was also studied.[39] Fe doping in Ga_2O_3 resulted in the formation of single-phase solid solution without any phase separation even up to x = 0.30 at. % Fe content, whereas W doping results in phase separation beyond x = 0.10 at. % W content. Moreover, these studies deal with charge balanced compounds due to isovalency of Ga, Fe, and W. Hence, in the present report we were inclined to develop charge imbalanced compounds by doping with aliovalent Ti^{4+} and study the dopant influence on crystal structure, microstructure, chemical bonding, and optical properties of Ti:β-Ga_2O_3 bulk ceramics. The impetus to choose Ti dopant in this study is 2-fold: (a) Shannon ionic radii[40] of Ti^{4+} in both octahedral and tetrahedral coordination (0.605 Å, 0.42 Å) closely matches with Ga^{3+} (0.62 Å, 0.47 Å), and (b) TiO_2 is a proven and promising candidate for applications including, viz., solar cells, sensing, photocatalyst, and optoelectronic devices.[41−44] The promising properties of TiO_2 may induce novel properties in Ti:β-Ga_2O_3 compounds;for example, a recent report on Ti-doped β-Ga_2O_3 single crystals proposes that these compounds might be potential candidates for ultrafast and tunable lasers.[45] Moreover, similar to Ga_2O_3, TiO_2 also exhibits different polymorphic phases in nature (anatase, rutile, brookite, and TiO_2(B)) with band gap ranging from 3.0 to 3.2 eV.[41,46,47] In doped compounds phase transitions associated with polymorphs greatly influence the structural and optical properties of the parent phase (in this study, Ga_2O_3). Hence, this work mainly focused on understanding and establishing the correlation between chemical inhomogeneity, insolubility, structural characteristics, and anomalies associated with optical properties of Ti:β-Ga_2O_3 bulk ceramics. Here, we have selectively chosen a mixed-phase precursor of TiO_2 (80% anatase + 20% rutile) to synthesize GTO compounds; this precursor is considered as an exceptional photocatalyst compared to single-phase compounds.[47] We believe this detailed study will be helpful for realizing new optoelectronic device applications based on β-Ga_2O_3. Moreover, recent studies indicate that Ga_2O_3 has high utility as a photocatalyst for the creation of H_2 fuel, especially through water splitting.[48] In addition, the photocatalytic activity of other polymorphs of Ga_2O_3 has been studied. Zhang et al. demonstrated that γ-Ga_2O_3 nanoparticles synthesized from solvothermal process exhibit enhanced photocatalytic activity when these nanoparticles incorporated into liquid metal/metal oxide frameworks made of micro-nanosized galinstan spheres.[6] Moreover, hexagonal α-Ga_2O_3 nanoflakes derived from liquid metal gallium via sonication and subsequent annealing exhibit photocatalytic activity.[49] The enhanced photocatalytic activity of these nanoflakes was attributed to a narrowed band gap (1.65 eV) resulting from trap states. Hence, in this report we also made an attempt to explore the electrocatalytic activity of titanium-doped gallium oxide toward hydrogen evolution reaction.

2. EXPERIMENTAL DETAILS

2.1. Synthesis. The conventional high-temperature solid state reaction was used to synthesize Ti-doped compounds ($Ga_{2-2x}Ti_xO_3$ (GTO; $0 \le x \le 0.2$). To synthesize GTO compounds, high-quality precursors (Ga_2O_3, TiO_2 (anatase + rutile)) were procured from Sigma-Aldrich with purities 99.99% and 99.9%, respectively. The high-purity precursors were weighed in stochiometric proportions to synthesize the respective compound. Stoichiometrically weighed precursor powders were homogeneously pulverized in an agate mortar with acetone as a wetting medium; a homogeneous mixture of GTO compounds was created. Usually 60−90 min of time was allocated for the pulverization of GTO compounds to enhance

https://dx.doi.org/10.1021/acs.cgd.9b00747
Cryst. Growth Des. 2020, 20, 1422−1433

homogeneity. After pulverization, compounds were calcined at different temperatures 1050, 1150, and 1250 °C for 12 h with intermediate pulverization to complete the reaction and to determine the optimal solubility limit. Having performed the phase analysis of calcined powders, powders were pelletized in the form of circular disc by adding binder (2% poly(vinyl alcohol) (PVA)). Circular disc pellets of 8 mm diameter and 1 mm thickness were pressed out from a MTI hydraulic press by applying a load of 1.5 tons. These green pellets were then sintered at 1350 °C for 8 h with binder burnout carried out at 500 °C (30 min). Once the pellets were sintered, the final properties were derived from sintered pellets/powders.

2.2. Characterization. *X-ray Diffraction (XRD).* A Rigaku Benchtop powder XRD-Mini Flex II was used to analyze the composition and crystal structure of ceramics. The patterns collected from the diffractometer were calibrated to record from 10° to 80° of 2θ range. Step size was kept at 0.02° with a scan rate of 0.6°/min. Furthermore, Rietveld structural refinement single-phase compounds carried out using Fullprof Software.

Scanning Electron Microscopy (SEM). Microstructural features were obtained using the Hitachi-4800 scanning electron microscope. SPI sputter coating module was used to coat gold over the pellets for improved imaging.

X-ray Photoelectron Spectroscopy (XPS). The chemical analysis of the as-prepared GTO compounds was examined by employing X-ray photoelectron spectroscopy. All of the samples were mounted on a Cu stub using double-sided Cu tape and analyzed using a calibrated Kratos Axis Ultra DLD spectrometer (Kratos Analytical, Manchester, U.K.), which has a high-performance Al Kα (1486.7 eV) spherical mirror analyzer. A piece of Cu tape was attached to the sample surface connecting the stub in order to avoid charging issues (e.g., peak broadening, peak shifting, and so on), though charge neutralizer was used to compensate for the remnant surface charging effects. Survey and high-resolution (HR) scans were collected at pass energies of 160 and 40 eV, respectively. Surveys were obtained over the binding energy (BE) range of −5 to +1400 eV with a step size of 0.5 eV, whereas HR scans were obtained with a step size of 0.1 eV. The analysis area (i.e., 700 × 300 μm^2) is referred to as the full width at half-maximum (fwhm) of 0.78 eV for Ag $3d_{5/2}$ collected at 40 eV pass energy. HR scans were obtained for Ga 2p, Ga 3d, Ti 2p, O 1s, and C 1s peaks. Each HR scan was recorded for at least 16 sweeps in order to get well-resolved spectra. Both spectra (i.e., survey and HR) were collected under ultrahigh-vacuum (UHV; 4×10^{-9} Torr) condition. C 1s binding energy at 285 eV was used for the charge reference. Both spectra (i.e., survey and HR) were analyzed using CasaXPS V2.3.16 to obtain the atomic composition and more involved studies, respectively. Peaks were fitted by employing both Gaussian/Lorentzian (GL(30)) line shape and Shirley background subtraction, whereas compositional analysis was performed by employing the relative sensitivity factors for the instrument. At least three positions were chosen per sample in order to maintain the good statistical index. The estimated error for calculating the atomic concentrations of Ga, Ti, and O is considered ±0.01 at. % in this report

UV−Visible Spectroscopy. The optical absorption spectra were obtained from a JASCO made UV−vis spectrophotometer. Optical spectra are highly influenced by impurities, crystal symmetry, and defects. It is even influenced by the nature of hybridization between atomic orbitals for any given compound. Hence it is quite essential to understand the optical absorption spectra to gain valuable insights into elemental doping of a system.

Electrochemical Characterization. The electrocatalytic activity of Ti-doped Ga_2O_3 toward the hydrogen evolution reaction (HER) was evaluated using a three-electrode system using 0.5 M H_2SO_4(aq) electrolyte. Linear sweep voltammetry (CHI 6273E potentiostat) with scan rate of 50 mV s^{-1} was conducted using Ag/AgCl reference electrode and platinum as the counter electrode. For preparing the working electrode, powdered samples were mixed well in 80 μL of 5 wt % Nafion 117 solution (Sigma-Aldrich) through sonication. Subsequently, 20 μL of the above solution was drop cast onto a freshly polished glassy carbon working electrode, and the redox properties were analyzed in the 0 to −1.5 V voltage range.

2.3. Computational Methodology. We use density functional theory as implemented in the VASP code,[50] using projector augmented wave potentials[51] with an energy cutoff of 400 eV and a 2 × 2 × 2 **k**-point grid using a 120-atom supercell, corresponding to the 1 × 3 × 2 supercell of the conventional unit cell.[52] To accurately model the electronic and structural properties of Ga_2O_3, we use the HSE06 hybrid functional,[53] with a mixing parameter of 32%. Ga d electrons are included in the valence, as this was found to be important to accurately describe the ground state of Ga_2O_3 and the preferential positions of Al in Ga_2O_3.[54,55] All atomic positions are fully relaxed so that the remaining forces are smaller than 0.01 eV/Å. Formation energies were obtained using the formalism outlined in ref.56, where we referenced the chemical potentials of Ga to bulk metal and those of O to the O_2 molecule. Ga-rich and O-rich conditions were defined by the enthalpy of formation of Ga_2O_3. The chemical potential of Ti was determined by equilibrium with rutile/anatase TiO_2, corresponding to the solubility limit.

3. RESULTS AND DISCUSSION

3.1. Phase and Structural Analysis. The X-ray diffraction patterns of samples calcined at initial calcination temperature, i.e., 1050 °C (not shown here) revealed a high quantity of unreacted secondary phase corresponding to TiO_2. Hence, calcination was carried out at higher temperatures 1150 and 1250 °C. The XRD patterns of GTO compounds calcined at 1150 and 1250 °C are shown in Figure 1a,b, respectively. It is evident that all of the samples exhibit traces of TiO_2. The volume fractions of anatase and rutile phases were determined from the X-ray diffraction pattern of the TiO_2 as-received precursor from 100% intensity Bragg reflections of anatase (101) (25.32°) and rutile (110) (27.44°) using the following equations.[57,58]

$$\text{volume fraction of anatase} = \frac{I_{A(101)}}{(I_{A(101)} + I_{(110)})} \quad (1)$$

$$\text{volume fraction of rutile} = \frac{I_{R(110)}}{(I_{A(101)} + I_{(110)})} \quad (2)$$

From the above equations the obtained volume fractions of anatase and rutile phases are approximately equal to 80% and 20%, respectively.

From Figure 1a (calcined at 1150 °C), the X-ray diffraction patterns clearly show the presence of a secondary rutile phase even at low concentration (5 at. %) of Ti doping. However, there is no signature of unreacted anatase phase in all of the synthesized compounds. The intensity of the Bragg reflection corresponding to the rutile phase gradually increases, which is due to the non-equilibrium nature of the anatase phase and provision of conversion into a stable rutile phase between 600 and 1000 °C. Further samples were calcined at 1250 °C in order to estimate the optimal solubility limits of Ti into the Ga_2O_3 parent matrix. The diffraction pattern is indexed with respect to intrinsic Ga_2O_3 monoclinic symmetry.[37]

Figure 1b represents X-ray diffraction patterns of samples calcined at 1250 °C and precursor TiO_2. From diffraction patterns, it is clearly evident that there is formation of the single-phase Ti:Ga_2O_3 compound at lower concentration (5 at. %) of Ti doping, whereas beyond 5 at. % Ti doping results in formation of an unreacted TiO_2 rutile phase. However, Shannon ionic radii of Ti^{4+} and Ga^{3+} closely match in both tetrahedral and octahedra coordination.[40] We calculated the formation enthalpy of TiO_2 to be −9.17 eV and of Ga_2O_3 to be −10.47 eV, so very similar formation energies. Hence, the difference in formation enthalpies can be ruled out for

https://dx.doi.org/10.1021/acs.cgd.9b00747
Cryst. Growth Des. 2020, 20, 1422−1433

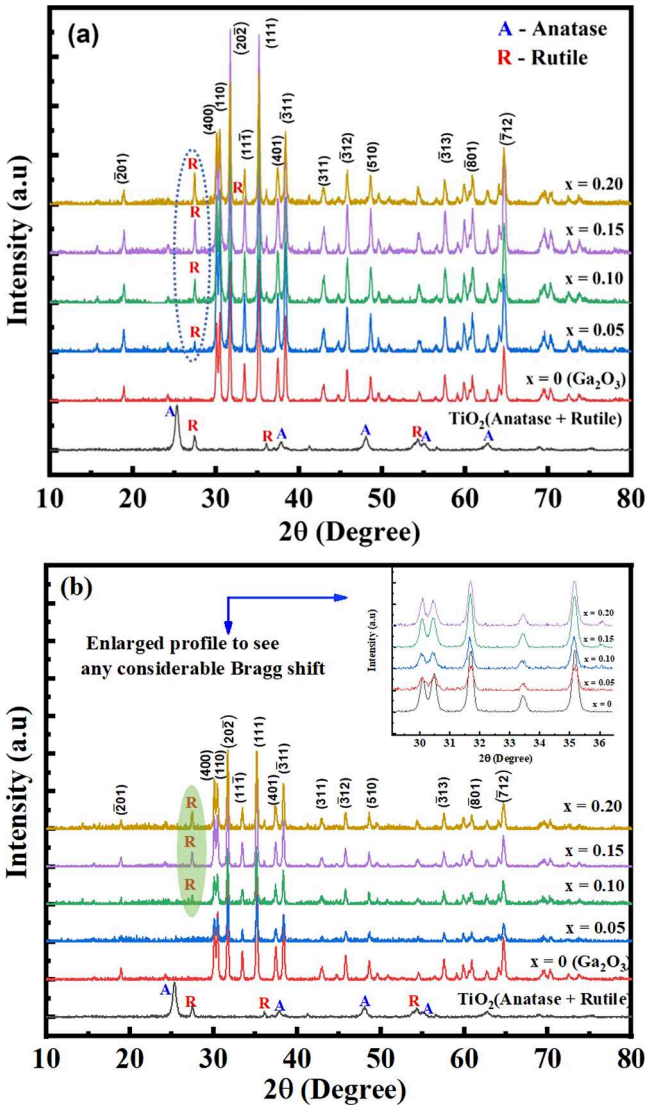

Figure 1. (a) X-ray diffraction patterns of synthesized compounds calcined at 1150 °C and as received precursor TiO_2. (b) X-ray diffraction patterns of synthesized compounds calcined at 1250 °C and as received precursor TiO_2.

insolubility. Moreover, electronegativities of Ti^{4+} (1.5) and Ga^{3+} (1.8) are in close proximity. So, it is worthwhile to mention the aliovalent characteristics of Ti $^{4+}$ and Ga^{3+} would be a possible reason for insolubility of Ti into the Ga_2O_3 matrix phase. Here, we have determined the volume fraction of the unreacted TiO_2 phase from 100% intensity Bragg reflections of rutile TiO_2 (110) and Ga_2O_3 (111) using the following equation.[57,58]

$$\text{volume fraction of } TiO_2 \text{ phase} = \frac{I_{RTiO_2(110)}}{(I_{Ga_2O_3(111)} + I_{RTO_2(110)})} \quad (3)$$

Estimated volume fractions of the rutile phase in mixed phase compositions of $x = 0.10$, $x = 0.15$, and $x = 0.20$ are 7.7%, 11.8%, and 13.9%, respectively. The estimated volume fraction of the rutile phase is nearly corroborated with stoichiometric calculations. In Figure 1b peaks corresponding to the rutile phase are highlighted by a vertical green solid oval to enhance the visibility for the reader. Enlarged X-ray diffraction profiles of high-intensity peaks are shown in the inset of Figure 1b to verify the Ti induced shift in the Bragg position. From the inset, there is no prominent shift in Bragg position but there is a small shift toward lower Bragg angle in Ti-doped compositions. However, the smaller ionic radii of Ti^{4+} compare to those of Ga^{3+} should lead to a shift in the Bragg position toward higher Bragg angle. The contradiction between the shift in the Bragg position and ionic radii might be due to Ti induced local structural disorder that resulted by global charge imbalance.

Figure 2 shows the X-ray diffraction patterns of samples sintered at 1350 °C for 8 h. In sintered compounds with high

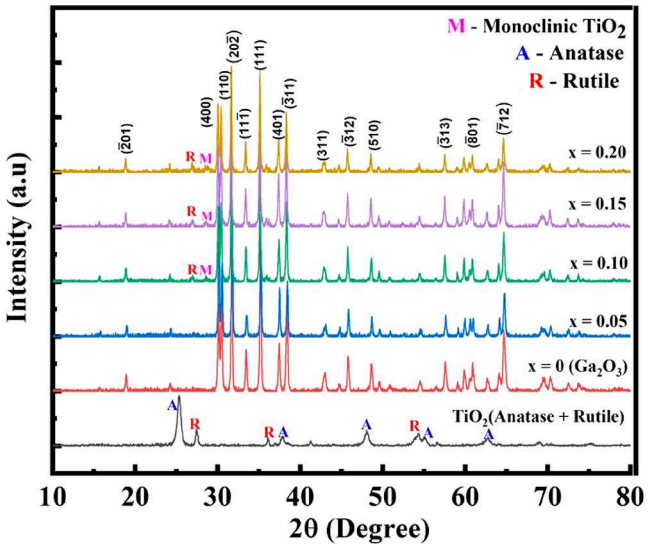

Figure 2. X-ray diffraction patterns of sintered powders at 1350 °C and as received precursor TiO_2.

Ti content, the Bragg reflection of the rutile phase around 27.44° shifts toward lower Bragg angle (26.87°). Such a shift in the Bragg position may be attributed to thermal expansion of the lattice. The volume fraction of unreacted rutile phase after sintering is estimated using eq 3. The estimated volume fractions of undissolved rutile TiO_2 phase in doped compounds with Ti concentration ≥ 10 at. % are 4.0% (x = 0.10), 4.8% (x = 0.15), and 6.4% (x = 0.20). Moreover, in sintered compounds we have noticed another secondary peak around 28.43°. This secondary peak closely matches with monoclinic TiO_2 (PDF No. 03-065-6429) with space group $P2_1/m$. Hence, it is evident that the fraction of undissolved rutile TiO_2 transforms into a metastable monoclinic phase due to the high-temperature sintering process. As a consequence, the volume fraction of undissolved rutile phase is decreased in sintered compounds compared to calcined compounds.

The crystal symmetries of single-phase compounds, intrinsic Ga_2O_3 and Ti-doped Ga_2O_3 (5 at. %), are verified through Rietveld analysis of diffraction patterns. Figure 3 represents refined patterns of intrinsic and doped compounds (x = 0.05) sintered at 1350 °C. The refinement of experimental patterns was carried out using a monoclinic model of intrinsic Ga_2O_3 with space group ($C2/m$). The goodness of fit (χ^2) of refined patterns reveals that both intrinsic and doped compounds are stabilized in monoclinic phase. The obtained structural parameters are shown in Table 1.

3.2. Computational Analysis. Our calculations reveal that Ti atoms preferentially substitute on the octahedrally

https://dx.doi.org/10.1021/acs.cgd.9b00747
Cryst. Growth Des. 2020, 20, 1422−1433

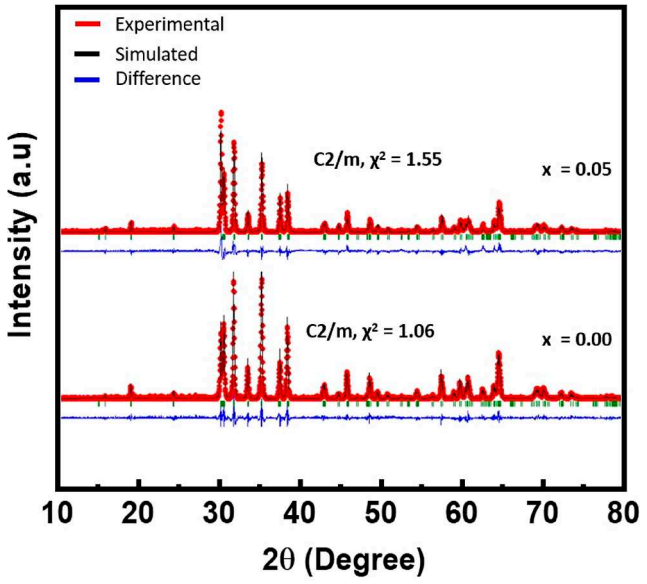

Figure 3. Reitveld refinement of intrinsic Ga_2O_3 and Ti-doped compound (x = 0.05) sintered at 1350 °C.

Table 1. Structural Parameters of GTO Compounds (x = 0.00 and 0.05)

		atomic coordinate			
Ti concn	atom	X	Y	Z	U_{iso}
0.00	Ga1	0.09104	0.00000	0.79590	0.00772
	Ga2	0.15858	0.50000	0.31332	0.00432
	O1	0.16257	0.00000	0.11307	0.0080
	O2	0.17048	0.00000	0.57658	−0.00077
	O3	−0.0037	0.50000	0.25023	−0.0050
0.05	Ga1	0.09180	0.00000	0.79140	0.01749
	Ga2	0.15472	0.50000	0.31218	0.00302
	O1	0.1484	0.00000	0.1511	0.01092
	O2	0.1549	0.00000	0.5989	−0.0020
	O3	−0.0354	0.50000	0.2410	−0.05684
	Ti1	0.09180	0.00000	0.7914	0.01749
	Ti2	0.15472	0.50000	0.31218	0.00302

coordinated Ga sites, with an energy difference compared to tetrahedrally coordinated sites of 0.90 eV for the 0 charge state and 0.37 eV for the 1+ charge state, as shown in Figure 4.

For both configurations, Ti will behave as a deep donor: for Fermi levels up to 3.42 eV (3.95 eV) above the valence-band maximum the octahedral (tetrahedral) Ti occurs in the 1+ charge state, indicating that it donates an electron to the conduction band. For larger Fermi levels, the Ti dopants will remain neutral.

Note that for Fermi levels up to 0.5 eV above the valence-band maximum, hole polarons can form, similar to what was found for other transition metal dopants.[59] Since these correspond to a 1+ charge state with one- or two-hole polarons and not a natural charge state, these are not shown in Figure 4.

3.3. Morphology. Figure 5 represents the scanning electron microscopic images of samples $Ga_{2-2x}T_xO_3$ ($0 \le x$ 0.15) sintered at 1350 °C for 8 h. Intrinsic Ga_2O_3 exhibits rod-like grain morphology, whereas doped compounds exhibit nearly spherical morphology. In intrinsic Ga_2O_3, grain boundary connectivity with adjacent grains was discontinuous;

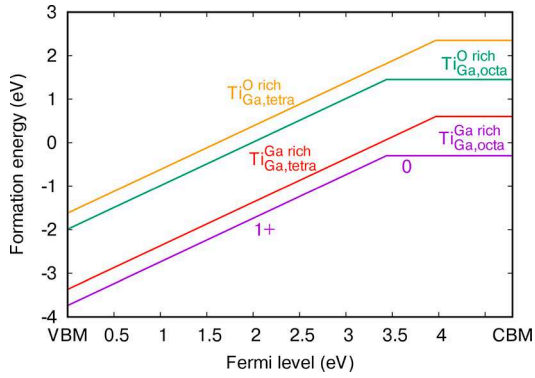

Figure 4. Formation energy diagram of substitutional Ti on octahedral and tetrahedral Ga sites as a function of the Fermi level, starting from the valence-band maximum (VBM) to the conduction-band minimum (CBM). Slopes indicate the charge state, as also indicated by the labels "0" and "1+". Both Ga-rich and O-rich conditions are shown.

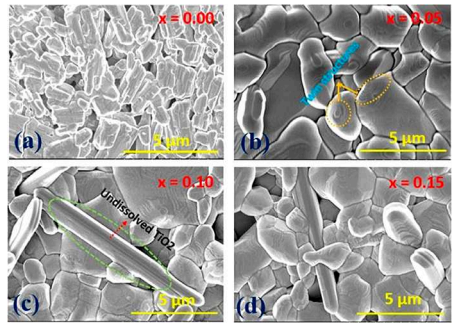

Figure 5. Scanning electron microscopy images of $Ga_{2-2x}T_xO_3$ [$0 \le x$ 0.15] samples sintered at 1350 °C.

the agglomerated grains or particles are found in certain regions. However, Ti doping drastically changes the morphology from rod-like shape to nearly spherical grains. The approximate grain sizes in intrinsic Ga_2O_3 varies in the range 1−3 μm, whereas the increment in grain size is evident in doped compounds, which is approximately up to 5 μm. The abnormal grain growth was noticed in Ti-doped compounds; such abnormal grain growth was attributed to defects induced by enhanced mass transport.[60−62]

Interestingly lattice twinning induced striations are found in Ti-doped compounds in contrast to intrinsic Ga_2O_3. Such twinning in doped compounds is attributed to anisotropic grain growth along specific crystallographic orientation.[37,63] The density of twinning induced striations increases with increasing Ti content. In addition, in accordance with phase analysis by X-ray diffraction (Figure 2), the unreacted TiO_2 segregated in the matrix phase as rod shaped morphology. Due to segregation of TiO_2 the discontinuity in the matrix phase resulted in relatively porous morphology in undissolved compounds.

Figure 6 represents energy dispersive X-ray spectroscopic mapping and spectra of two selected compositions. Mapping clearly shows uniform distribution of Ti, Ga, and O elements in a single-phase compound (x = 0.05), whereas, in the undissolved compounds, the absence of Ga was noticed in regions with segregated TiO_2. The TiO_2 region in mapping also corroborates with rod shaped morphology (shown in the figure). EDS spectra (Figure 6c,d) reveal that in accordance

https://dx.doi.org/10.1021/acs.cgd.9b00747
Cryst. Growth Des. 2020, 20, 1422−1433

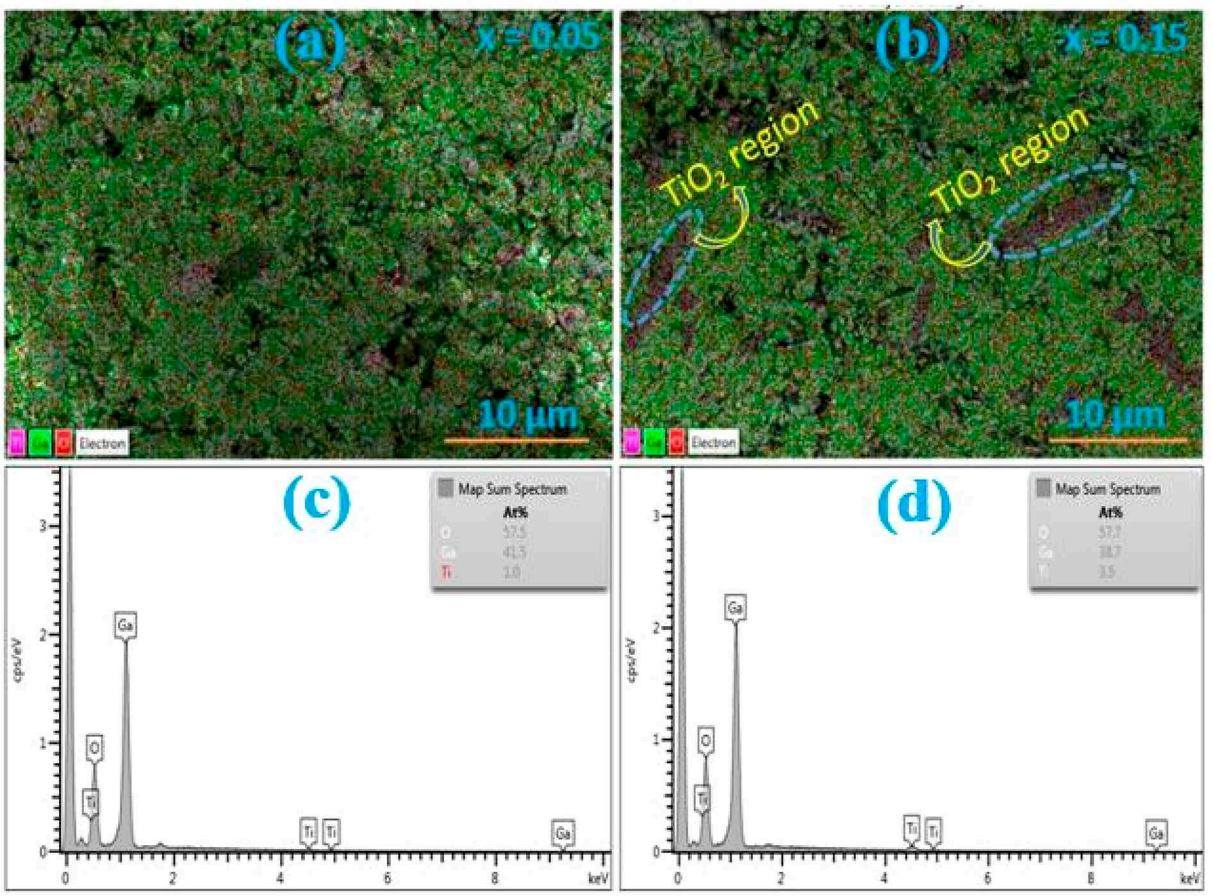

Figure 6. Electron dispersive spectroscopic mapping and spectra of two selected compositions.

with the stoichiometry the intensity of the Ti peak increases with increasing Ti content.

3.4. Chemical Bonding. Figure 7 represents the survey spectra of the GTO compounds. The survey spectra clearly show core level peaks correspond to Ga 2p, O 1s, C 1s, Ga 3d, Ga 3s, Ti 2p, and Auger lines (Ga LMM, O KLL). In the survey scan, at lower concentrations of Ti doping the intensity of the Ti 2p peak is not prominent but at x = 0.20 it shows considerable intensity with clear visibility. The position of the Ti 2p peak is represented with a dotted red line. Hence, we have recorded high-resolution spectra of Ga 2p, O 1s, and T 2p peaks to explore changes associated with chemical bonding and binding energy due to Ti doping.

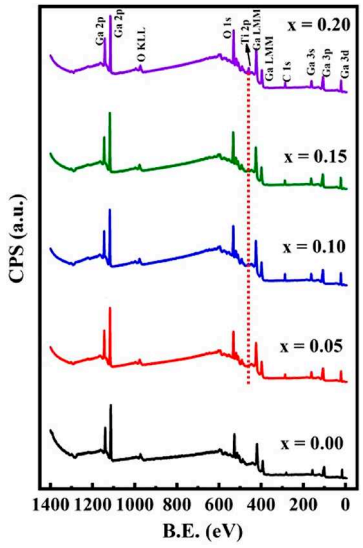

Figure 7. XPS survey spectra of $Ga_{2-2x}Ti_xO_3$ ($0 \leq x \leq 0.2$) compounds sintered at 1350 °C.

Figure 8a represents the high-resolution spectra of Ga 2p. Ga 2p exhibits doublet characteristics corresponding to Ga $2p_{3/2}$ and Ga $2p_{1/2}$ with BEs 1117.6 and 1144.5 eV, respectively. Understanding the behavior of Ga 2p peaks provides information about Ti doping induced changes associated with Ga−O chemical bonding and Ga valence state in the synthesized GTO compounds. The reported BE values of Ga $2p_{3/2}$ and Ga $2p_{1/2}$ in metallic Ga are 1117.0 and 1144.0 eV, respectively. It is evident from spectra that there is a positive shift of approximately 0.5 eV as compared to metallic Ga. The shift in the BE occurs mainly due to the redistribution of the electronic cloud around the constituent atoms.[64−66] On the basis of the derived information and validating with the available literature, it is inferred that Ga exists in trivalent state (i.e., Ga^{3+}) within these GTO compounds.[67]

High-resolution spectra of O 1s are depicted in Figure 8b. In all the synthesized compounds, including intrinsic Ga_2O_3, an asymmetry in peak shape is observed.[64] The O 1s peak resolved into two regions: (a) a main peak centered at 530.7 eV and (b) two small shoulder peaks located at higher binding energies at 532.2 and 533.4 eV. To represent the peak positions, in Figure 8b the main peak and peak at 533.4 eV are

https://dx.doi.org/10.1021/acs.cgd.9b00747
Cryst. Growth Des. 2020, 20, 1422−1433

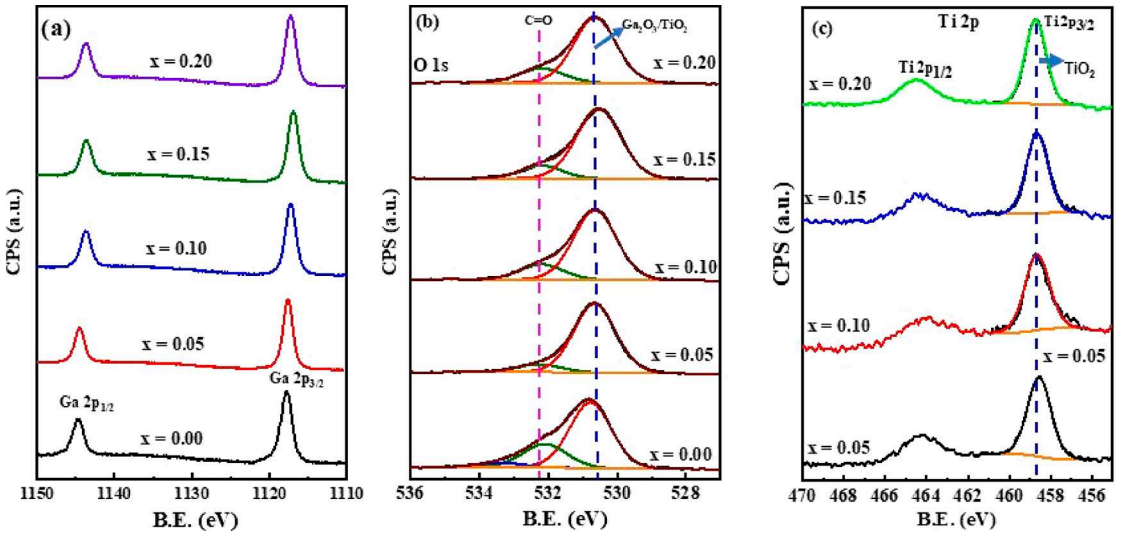

Figure 8. High-resolution XPS spectra of (a) Ga 2p, (b) O 1s, and (c) Ti 2p.

highlighted with blue and pink dotted lines, respectively. It has been reported in the literature that the O 1s peak for intrinsic Ga_2O_3 occurs generally at BE of 530.6 eV, whereas it occurs at 530.1 eV for intrinsic TiO_2. Hence, from the main peak at 530.7 eV, it is evident that there is no considerable variation in binding energy; however, peak broadening was noticed in Ti-doped compounds. The peak broadening in doped compounds might be due to interaction between Ga−O and Ti−O chemical bonds. The shoulder peaks at BE 532.2 and 533.4 eV attributed to O−C or O−H bonds on the surface of the sample. The adventitious carbon gets adsorbed on the sample surface during the sample transfer procedure from the furnace atmosphere to the XPS analysis chamber.[64]

The high-resolution Ti 2p spectra are shown in Figure 8c. Similar to Ga 2p, Ti 2p also exhibits doublet characteristics of Ti $2p_{3/2}$ and Ti $2p_{1/2}$, which appear at BE of 458.5 and 464.2 eV, respectively, for TiO_2. From BE values of Ti $2p_{3/2}$ and Ti $2p_{1/2}$, it is evident that Ti stabilizes in the tetravalent state (Ti^{4+}) in all of the GTO compounds.[68] The deconvolution of (fitting) Ti $2p_{3/2}$ results in a single peak, which confirms the absence of other valence states of Ti. Interestingly, we are unable to fit the Ti $2p_{1/2}$ peak. The possible reason for this is the obtained Ti $2p_{1/2}$ peak is broader with less intensity than is usually expected. Such broadening and less intensity of the Ti $2p_{1/2}$ peak are attributed to Coster−Kronig effect; due to this effect Ti $2p_{1/2}$ is a very short lived state compared to Ti $2p_{3/2}$ that resulted from post-ionization. Moreover, with increasing Ti concentration in the GTO compounds, the full width at half-maximum of the Ti $2p_{3/2}$ peak is decreased slightly from 1.35 to 1.2 eV, which is very usual in the case of Gaussian/Lorentzian (GL(30)) peak fitting, where ±0.2 eV is maintained as the error bar.

3.5. Optical Properties. Figure 9 represents the optical absorption spectra of $Ga_{2-2x}Ti_xO_3$ ($0 \le x \le 0.2$) compounds sintered at 1350 °C. Doped compounds exhibit two absorption edges in contrast to intrinsic Ga_2O_3, first around 300 nm and second around 400 nm; in the figure red and blue dotted ovals represent the same. The observed absorption edges in doped compounds are similar to those of intrinsic β-Ga_2O_3 and undissolved TiO_2. The red shift in the absorption edge was noted in both edges, but the red shift in the second absorption edge is not prominent. As mentioned earlier, a red shift in

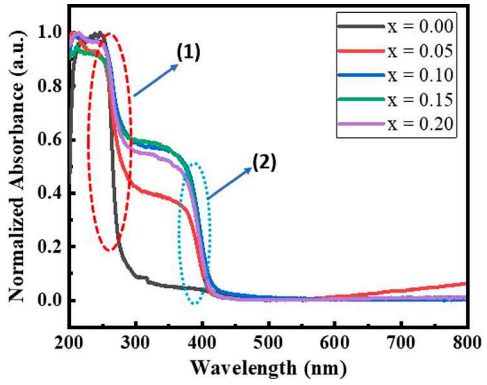

Figure 9. Optical absorption spectra of $Ga_{2-2x}Ti_{1x}O_3$ ($0 \le x \le 0.2$) compounds sintered at 1350 °C.

optical band gap is reported in polycrystalline thin films of Ti-doped compounds.[29] However, in doped compounds the optical band gap mainly depends on changes associated with electronic structure (hybridization of atomic orbitals of constituent elements of the compound), changes in orbital contributions to valence band and conduction band, defects, and secondary phases and/or undissolved phases.

Further, Ga_2O_3 is known to exhibit both direct and indirect band gaps, whereas rutile TiO_2 exhibits an indirect band gap and anatase TiO_2 an indirect band gap. Hence, we have estimated band gap values using the well-known Tauc method.[69,70] The Tauc equation is given by

$$\alpha h\nu = A(h\nu - E_g)^n \quad (4)$$

where α is an absorption coefficient, $h\nu$ an incident photon energy, A a proportionality constant, $E_g$the band gap, n a constant that determines the type of band gap. $n = 1/2$ represents a direct allowed transition, $n = 2$ represents an indirect allowed transition, $n = 3/2$ represents a direct forbidden transition, and $n = 3$ represents an indirect forbidden transition. Figure 10a represents the Tauc plot of a direct allowed transition. In Figure 10a,b, extrapolation of the linear portion of absorption edges to x-coordinate gives the band gap values. The direct band gap values vary from 4.6 eV (intrinsic Ga_2O_3) to 4.2 eV. The titanium doping induces a red shift of

https://dx.doi.org/10.1021/acs.cgd.9b00747
Cryst. Growth Des. 2020, 20, 1422−1433

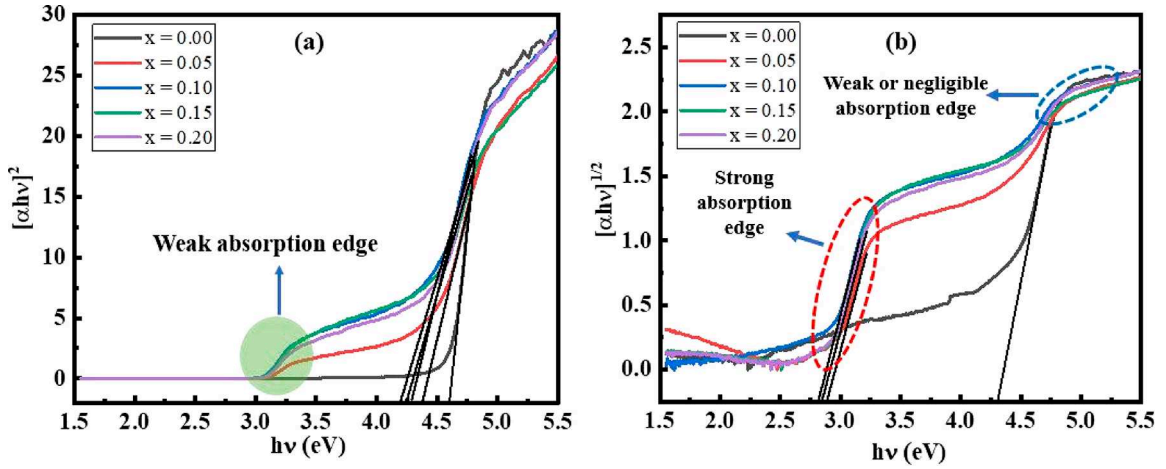

Figure 10. Tauc plots of $Ga_{2-2x}Ti_xO_3$ ($0 \leq x \leq 0.2$) compounds: (a) direct band gap and (b) indirect band gap.

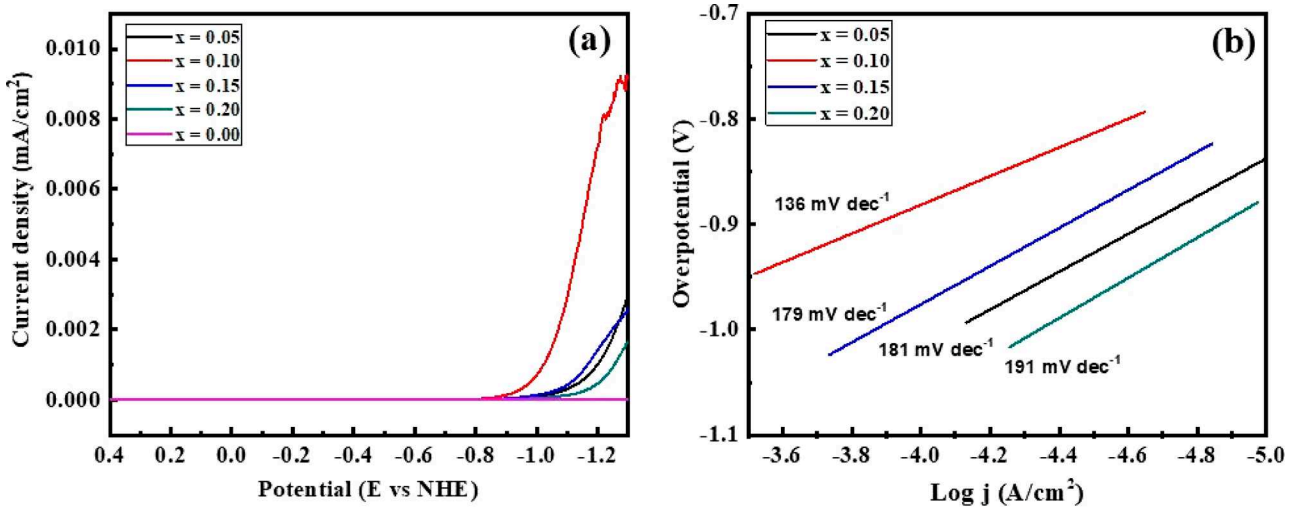

Figure 11. Electrochemical characterization of the doped and undoped Ga_2O_3. (a) Polarization curves obtained at 50 mV s^{-1} scan rate and (b) Tafel slopes for Ti-doped samples.

0.4 eV in the GTO compounds. But the weak second absorption was evident from Figure 10a (green circled). The second absorption edge in Ti:Ga_2O_3 compounds is the resultant of TiO_2 chemical inhomogeneity and/or phase separation. From Figure 9 it is clearly noticed that the first absorption in doped compounds is weak (in the figure represented as a blue dotted oval), whereas the second absorption is prominent and strong (in the figure represented as a red dotted oval). The strong second absorption is mainly due to undissolved TiO_2. The band gap value of undissolved TiO_2 is approximately 2.8 eV; the lower band gap value TiO_2 than expected is due to high-temperature processing induced lattice strains and defects. Assigning this absorption edge to TiO_2 is consistent with the expected band alignment. Combining the experimental electron affinity of TiO_2 (4 eV)[71] with a calculated electron affinity of Ga_2O_3 of 3.90 eV[54] shows that the band alignment is of type I, with the band edges of TiO_2 within the band gap of Ga_2O_3. Moreover, it is evident that Ti doping induces a red shift of the direct gap of intrinsic Ga_2O_3 with a strong absorption edge. The deep donor level of Ti in Ga_2O_3 is not directly responsible for the observed red shift: we expect the crystal to be unintentional n-type doped, which means that the Fermi level will be close to the conduction-band edge. In that case, Ti will be in the 0 charge state (see Figure 4), so that the defect level will be filled. Since the level is filled, no optical transitions from the valence band to the defect level can take place. Unpopulating this level requires shifting the Fermi level much lower, requiring deliberate doping with compensating defects, such as Mg and N.[23] The small red shift of the direct absorption is therefore more likely caused by other effects, such as strain effects due to the TiO_2 inclusions and Ti doping induced structural changes. On the basis of the overall analysis, we believe Ti doping of Ga_2O_3 might be useful for realizing new optical electronic device applications based on Ga_2O_3.

3.6. Electrocatalytic Activity. The comparatively wide band gap, as well as negligible catalytic response from Ga-based active centers, limits the application of β-Ga_2O_3 as electrocatalysts or photocatalysts. The lattice incorporation (doping) of Ti in the present study serves the dual purpose of engineering the band gap and introducing highly catalytic (Ti) centers into Ga_2O_3. While the exploration of β-Ga_2O_3 as photocatalysts for the creation of H_2 fuel through water splitting witnessed some progress,[41] its use (either in native state or in doped configuration) as an electrocatalyst is severely underexplored. Doping Ti into materials demonstrated a great

https://dx.doi.org/10.1021/acs.cgd.9b00747
Cryst. Growth Des. 2020, 20, 1422−1433

capacity to improve photo- and electrochemical properties.[72,73] Hence, we investigated the cumulative effect of band structure modification and introduction of new catalytic centers in doped β-Ga_2O_3 samples, taking hydrogen evolution reaction as the model electrocatalytic process. Figure 11a illustrates the effect of different doping concentrations of Ti on the electrocatalytic activity of β-Ga_2O_3. The intrinsic Ga_2O_3 did not exhibit any electrocatalytic activity in aerobic conditions within the potential range explored in the study. However, we can see the significant electrocatalytic nature of the $Ga_{2-2x}Ti_xO_3$-doped samples with the highest activity when x = 0.10, with an onset potential of 860 mV. By fitting the linear portions of the Tafel plots to the Tafel equation ($\eta = b \log j + a$, where j is the current density and b is the Tafel slope), the slope of 136 mV per decade was obtained for x = 0.10 $Ga_{2-2x}Ti_xO_3$ (Figure 11b). The lower onset potential and Tafel slope, in combination with a higher current density, implies the superiority of $Ga_{2-2x}T_xO_3$ (x = 0.10) toward HER. The observed enhancement in the activity of Ti-doped Ga_2O_3 can plausibly be attributed to the availability of more catalytically active sites, where the Ti doping retains its additional electron (in n-type conditions). The doped metal atom on the surface can promote the water dissociation step of HER by decreasing the free-energy barrier for the transformation of H^+ ions to H_2. It is imperative to note that the direct band gap of β-Ga_2O_3 decreases due to Ti doping, which in turn facilitates more comfortable proton reduction. Nevertheless, the electrocatalytic activity does not follow a linear relationship with doping. We hypothesize that the optimum positioning of the bands that enables faster HER is obtained for the $Ga_{2-2x}Ti_xO_3$ with x = 0.10, while further increase in doping concentration shifts the band alignment. Hence, we attribute the overall enhancement to the synergistic effect of electronic effect (energy level matching) and rich active sites. Our results indicate that engineering the electron density of β-Ga_2O_3 via metal doping can significantly influence the electrocatalytic activity of β-Ga_2O_3 and tuning the doping concentration as well as the size and shape of the base material can derive highly efficient Ga_2O_3-based electrocatalysts.

4. CONCLUSIONS

$Ga_{2-2x}Ti_xO_3$ (GTO) ($0 \le x \le 0.20$) compounds were synthesized using a conventional high-temperature solid state reaction route. The samples were calcined at different temperatures 1050, 1150, and 1250 °C. X-ray diffraction of calcined samples at 1250 °C reveals that at low concentrations of Ti ≤ 5 at. % results single-phase formation, whereas beyond 5 at. % a significant undissolved TiO_2 rutile phase was present. Samples were sintered at 1350 °C; from X-ray diffraction of sintered samples it is evident that a fraction of undissolved TiO_2 rutile phase transforms into monoclinic TiO_2 phase. In sintered samples mixed undissolved phase (rutile + monoclinic) is present in samples with Ti content beyond 5 at. %. Crystal symmetry of intrinsic and single-phase compound was examined using Rietveld method. Rietveld analysis of intrinsic β-Ga_2O_3 and single-phase compound (x = 0.05) confirms that compounds are stabilized in monoclinic symmetry with $C2/m$ space group. Microstructural features of samples reveal that intrinsic β-Ga_2O_3 exhibits rod shaped morphology and doped compounds exhibit spherical morphology. Doped compounds exhibit abnormal grain growth, and twin structures resulted by enhanced mass transport and anisotropic abnormal grain growth, respectively. Moreover, the density of twin structures increases with increasing Ti concentration. High-resolution XPS of Ga 2p reveals that a positive shift in peak position as compared to metallic Ga resulted from electron cloud redistribution of adjacent atoms, and anomalous broadening in Ti $2p_{1/2}$ was noticed due to the Coster−Kronig effect. Ti behaves as a deep donor in Ga_2O_3 and preferentially substitutes on octahedral sites. The optical properties of GTO compounds reveal that Ti induces a red shift in direct allowed transition. A strong absorption within the Ga_2O_3 band gap is evident in doped compounds with Ti concentration ≥ 0.10 at. %, and consistent with a type 1 alignment, where the band edges of TiO_2 are within Ga_2O_3's band gap. Moreover, Ti-doped compounds exhibit electrocatalytic activity in contrast to β-Ga_2O_3; such electrocatalytic behavior of doped compounds is plausibly due to dopant induced catalytic sites.

AUTHOR INFORMATION

Corresponding Authors

Mallesham Bandi − *Center for Advanced Materials Research (CMR), University of Texas at El Paso, El Paso, Texas 79968, United States;* orcid.org/0000-0002-7875-3518; Email: mbandi@utep.edu

C. V. Ramana − *Center for Advanced Materials Research (CMR), University of Texas at El Paso, El Paso, Texas 79968, United States;* orcid.org/0000-0002-5286-3065; Email: rvchintalapalle@utep.edu

Authors

Vishal Zade − *Center for Advanced Materials Research (CMR), University of Texas at El Paso, El Paso, Texas 79968, United States*

Swadipta Roy − *Center for Advanced Materials Research (CMR) and Department of Metallurgical, Materials and Biomedical Engineering, University of Texas at El Paso, El Paso, Texas 79968, United States; Environmental Molecular Sciences Laboratory (EMSL), Pacific Northwest National Laboratory (PNNL), Richland, Washington 99352, United States*

Aruna N. Nair − *Department of Chemistry, University of Texas at El Paso, El Paso, Texas 79968, United States*

Sierra Seacat − *Department of Physics and Astronomy, University of Kansas, Lawrence, Kansas 66045, United States*

Sreeprasad Sreenivasan − *Department of Chemistry, University of Texas at El Paso, El Paso, Texas 79968, United States;* orcid.org/0000-0002-5728-0512

V. Shutthanandan − *Environmental Molecular Sciences Laboratory (EMSL), Pacific Northwest National Laboratory (PNNL), Richland, Washington 99352, United States;* orcid.org/0000-0003-2957-7535

Chris G. Van de Walle − *Materials Department, University of California, Santa Barbara, California 93106-5050, United States;* orcid.org/0000-0002-4212-5990

Hartwin Peelaers − *Department of Physics and Astronomy, University of Kansas, Lawrence, Kansas 66045, United States;* orcid.org/0000-0002-7141-8688

Complete contact information is available at: https://pubs.acs.org/10.1021/acs.cgd.9b00747

Author Contributions

[▽]M.B. and V.Z. contributed equally to this work.

Notes

The authors declare no competing financial interest.

https://dx.doi.org/10.1021/acs.cgd.9b00747
Cryst. Growth Des. 2020, 20, 1422−1433

■ ACKNOWLEDGMENTS

We acknowledge, with pleasure, support from the National Science Foundation (NSF) with NSF-PREM Grant No. DMR-1827745. Some of the work is also based upon work supported by the Air Force Office of Scientific Research under Award No. FA9550-18-1-0387. The computational work was supported by the GAME MURI of the Air Force Office of Scientific Research (Award No. FA9550-18-1-0479). Computing resources were provided by the Extreme Science and Engineering Discovery Environment (XSEDE), which is supported by National Science Foundation Grant No. ACI-1548562 (TG-DMR070072N). However, any opinions, finding, and conclusions or recommendations expressed in this material are those of the author(s) and do not necessarily reflect the views of the funding agencies. A portion of the research was performed using Environmental Molecular Sciences Laboratory (EMSL), a national scientific user facility sponsored by the Department of Energy's Office of Biological and Environmental Research and located at Pacific Northwest National Laboratory.

■ REFERENCES

(1) Passlack, M.; Hong, M.; Mannaerts, J. Quasistatic and high frequency capacitance−voltage characterization of Ga_2O_3−GaAs structures fabricated by in situ molecular beam epitaxy. *Appl. Phys. Lett.* **1996**, *68*, 1099−1101.

(2) Li, Z.; De Groot, C.; Moodera, J. H. Gallium oxide as an insulating barrier for spin-dependent tunneling junctions. *Appl. Phys. Lett.* **2000**, *77*, 3630−3632.

(3) Fu, L.; Liu, Y.; Hu, P. a.; Xiao, K.; Yu, G.; Zhu, D. Ga_2O_3 nanoribbons: synthesis, characterization, and electronic properties. *Chem. Mater.* **2003**, *15*, 4287−4291.

(4) Farvid, S. S.; Wang, T.; Radovanovic, P. V. Colloidal gallium indium oxide nanocrystals: a multifunctional light-emitting phosphor broadly tunable by alloy composition. *J. Am. Chem. Soc.* **2011**, *133*, 6711−6719.

(5) Ogita, M.; Saika, N.; Nakanishi, Y.; Hatanaka, Y. Ga2O3 thin films for high-temperature gas sensors. *Appl. Surf. Sci.* **1999**, *142*, 188−191.

(6) Zhang, W.; Naidu, B. S.; Ou, J. Z.; O'Mullane, A. P.; Chrimes, A. F.; Carey, B. J.; Wang, Y.; Tang, S.-Y.; Sivan, V.; Mitchell, A.; Bhargava, S. K.; Kalantar-zadeh, K. Liquid metal/metal oxide frameworks with incorporated Ga_2O_3 for photocatalysis. *ACS Appl. Mater. Interfaces* **2015**, *7*, 1943−1948.

(7) Zhang, X.; Huang, H.; Zhang, Y.; Liu, D.; Tong, N.; Lin, J.; Chen, L.; Zhang, Z.; Wang, X. Phase Transition of Two-Dimensional β-Ga_2O_3 Nanosheets from Ultrathin γ-Ga2O3 Nanosheets and Their Photocatalytic Hydrogen Evolution Activities. *ACS Omega* **2018**, *3*, 14469−14476.

(8) Lee, S. H.; Kim, S. B.; Moon, Y.-J.; Kim, S. M.; Jung, H. J.; Seo, M. S.; Lee, K. M.; Kim, S.-K.; Lee, S. W. High-responsivity deep-ultraviolet-selective photodetectors using ultrathin gallium oxide films. *ACS Photonics* **2017**, *4*, 2937−2943.

(9) Li, Y.; Tokizono, T.; Liao, M.; Zhong, M.; Koide, Y.; Yamada, I.; Delaunay, J. J. Efficient assembly of bridged β-Ga2O3 nanowires for solar-blind photodetection. *Adv. Funct. Mater.* **2010**, *20*, 3972−3978.

(10) Guo, D.; Liu, H.; Li, P.; Wu, Z.; Wang, S.; Cui, C.; Li, C.; Tang, W. Zero-power-consumption solar-blind photodetector based on β-Ga_2O_3/NSTO heterojunction. *ACS Appl. Mater. Interfaces* **2017**, *9*, 1619−1628.

(11) Orita, M.; Ohta, H.; Hirano, M.; Hosono, H. Deep-ultraviolet transparent conductive β-Ga2O3 thin films. *Appl. Phys. Lett.* **2000**, *77*, 4166−4168.

(12) Sinha, G.; Adhikary, K.; Chaudhuri, S. Effect of annealing temperature on structural transformation of gallium based nano-crystalline oxide thin films and their optical properties. *Opt. Mater.* **2007**, *29*, 718−722.

(13) Pearton, S. J.; Yang, J.; Cary, P. H., IV; Ren, F.; Kim, J.; Tadjer, M. J.; Mastro, M. A. A review of Ga_2O_3 materials, processing, and devices. *Appl. Phys. Rev.* **2018**, *5*, 011301.

(14) Stepanov, S.; Nikolaev, V.; Bougrov, V.; Romanov, A. Gallium oxide: properties and applications - A review. *Rev. Adv. Mater. Sci.* **2016**, *44*, 63−86.

(15) He, H.; Orlando, R.; Blanco, M. A.; Pandey, R.; Amzallag, E.; Baraille, I.; Rérat, M. First-principles study of the structural, electronic, and optical properties of Ga_2O_3 in its monoclinic and hexagonal phases. *Phys. Rev. B: Condens. Matter Mater. Phys.* **2006**, *74*, 195123.

(16) Geller, S. Crystal structure of β-Ga_2O_3. *J. Chem. Phys.* **1960**, *33*, 676−684.

(17) Tomm, Y.; Reiche, P.; Klimm, D.; Fukuda, T. Czochralski grown Ga_2O_3 crystals. *J. Cryst. Growth* **2000**, *220*, 510−514.

(18) Kyrtsos, A.; Matsubara, M.; Bellotti, E. On the feasibility of p-type Ga_2O_3. *Appl. Phys. Lett.* **2018**, *112*, 032108.

(19) Siah, S.; Brandt, R.; Lim, K.; Schelhas, L.; Jaramillo, R.; Heinemann, M.; Chua, D.; Wright, J.; Perkins, J. D.; Segre, C.; Gordon, R. G.; Toney, M. F.; Buonassisi, T. Dopant activation in Sn-doped Ga_2O_3 investigated by X-ray absorption spectroscopy. *Appl. Phys. Lett.* **2015**, *107*, 252103.

(20) Jaiswal, P.; Ul Muazzam, U.; Pratiyush, A. S.; Mohan, N.; Raghavan, S.; Muralidharan, R.; Shivashankar, S.; Nath, D. N. Microwave irradiation-assisted deposition of Ga_2O_3 on III-nitrides for deep-UV opto-electronics. *Appl. Phys. Lett.* **2018**, *112*, 021105.

(21) Higashiwaki, M.; Sasaki, K.; Kuramata, A.; Masui, T.; Yamakoshi, S. Gallium oxide (Ga2O3) metal-semiconductor field-effect transistors on single-crystal β-Ga2O3 (010) substrates. *Appl. Phys. Lett.* **2012**, *100*, 013504.

(22) Zhang, F.; Arita, M.; Wang, X.; Chen, Z.; Saito, K.; Tanaka, T.; Nishio, M.; Motooka, T.; Guo, Q. Toward controlling the carrier density of Si doped Ga_2O_3 films by pulsed laser deposition. *Appl. Phys. Lett.* **2016**, *109*, 102105.

(23) Peelaers, H.; Lyons, J. L.; Varley, J. B.; Van de Walle, C. G. Deep acceptors and their diffusion in Ga2O3. *APL Mater.* **2019**, *7*, 022519.

(24) Varley, J. B.; Weber, J. R.; Janotti, A.; Van de Walle, C. G. Oxygen vacancies and donor impurities in β-Ga_2O_3. *Appl. Phys. Lett.* **2010**, *97*, 142106.

(25) Ohira, S.; Suzuki, N.; Arai, N.; Tanaka, M.; Sugawara, T.; Nakajima, K.; Shishido, T. Characterization of transparent and conducting Sn-doped β-Ga_2O_3 single crystal after annealing. *Thin Solid Films* **2008**, *516*, 5763−5767.

(26) Suzuki, N.; Ohira, S.; Tanaka, M.; Sugawara, T.; Nakajima, K.; Shishido, T. Fabrication and characterization of transparent conductive Sn-doped β-Ga_2O_3 single crystal. *Phys. Status Solidi C* **2007**, *4*, 2310−2313.

(27) Víllora, E. G.; Shimamura, K.; Yoshikawa, Y.; Ujiie, T.; Aoki, K. Electrical conductivity and carrier concentration control in β-Ga_2O_3 by Si doping. *Appl. Phys. Lett.* **2008**, *92*, 202120.

(28) Feng, X.; Li, Z.; Mi, W.; Luo, Y.; Ma, J. Mg-doped β-Ga_2O_3 films with tunable optical band gap prepared on MgO (110) substrates by metal-organic chemical vapor deposition. *Mater. Sci. Semicond. Process.* **2015**, *34*, 52−57.

(29) Manandhar, S.; Ramana, C. Direct, functional relationship between structural and optical properties in titanium-incorporated gallium oxide nanocrystalline thin films. *Appl. Phys. Lett.* **2017**, *110*, 061902.

(30) Rubio, E.; Ramana, C. V. Tungsten-incorporation induced red-shift in the bandgap of gallium oxide thin films. *Appl. Phys. Lett.* **2013**, *102*, 191913.

(31) Battu, A. K.; Manandhar, S.; Shutthanandan, V.; Ramana, C. V. Controlled optical properties via chemical composition tuning in molybdenum-incorporated β-Ga_2O_3 nanocrystalline films. *Chem. Phys. Lett.* **2017**, *684*, 363−367.

https://dx.doi.org/10.1021/acs.cgd.9b00747
Cryst. Growth Des. 2020, 20, 1422−1433

(32) Binet, L.; Gourier, D. Origin of the blue luminescence of β-Ga_2O_3. *J. Phys. Chem. Solids* **1998**, *59*, 1241−1249.
(33) Wang, T.; Farvid, S. S.; Abulikemu, M.; Radovanovic, P. V. Size-tunable phosphorescence in colloidal metastable γ-Ga_2O_3 nanocrystals. *J. Am. Chem. Soc.* **2010**, *132*, 9250−9252.
(34) Wang, T.; Radovanovic, P. V. Size-dependent electron transfer and trapping in strongly luminescent colloidal gallium oxide nanocrystals. *J. Phys. Chem. C* **2011**, *115*, 18473−18478.
(35) Layek, A.; Yildirim, B.; Ghodsi, V.; Hutfluss, L. N.; Hegde, M.; Wang, T.; Radovanovic, P. V. Dual europium luminescence centers in colloidal Ga_2O_3 nanocrystals: controlled in situ reduction of Eu (III) and stabilization of Eu (II). *Chem. Mater.* **2015**, *27*, 6030−6037.
(36) Wang, T.; Layek, A.; Hosein, I. D.; Chirmanov, V.; Radovanovic, P. V. Correlation between native defects and dopants in colloidal lanthanide-doped Ga_2O_3 nanocrystals: a path to enhance functionality and control optical properties. *J. Mater. Chem. C* **2014**, *2*, 3212−3222.
(37) Zade, V.; Mallesham, B.; Shantha-Kumar, S.; Bronson, A.; Ramana, C. V. Interplay between Solubility Limit, Structure, and Optical Properties of Tungsten-Doped Ga_2O_3 Compounds Synthesized by a Two-Step Calcination Process. *Inorg. Chem.* **2019**, *58*, 3707−3716.
(38) Zade, V.; Mallesham, B.; Roy, S.; Shutthanandan, V.; Ramana, C. V. Electronic Structure of Tungsten-Doped β-Ga_2O_3 Compounds. *ECS J. Solid State Sci. Technol.* **2019**, *8*, Q3111−Q3115.
(39) Roy, S.; Mallesham, B.; Zade, V. B.; Martinez, A.; Shutthanandan, V.; Thevuthasan, S.; Ramana, C. V. Correlation between Structure, Chemistry, and Dielectric Properties of Iron-Doped Gallium Oxide ($Ga_{2-x}Fe_xO_3$). *J. Phys. Chem. C* **2018**, *122*, 27597−27607.
(40) Shannon, R. D. Revised effective ionic radii and systematic studies of interatomic distances in halides and chalcogenides. *Acta Crystallogr., Sect. A: Cryst. Phys., Diffr., Theor. Gen. Crystallogr.* **1976**, *32*, 751−767.
(41) Kapilashrami, M.; Zhang, Y.; Liu, Y.-S.; Hagfeldt, A.; Guo, J. Probing the optical property and electronic structure of TiO_2 nanomaterials for renewable energy applications. *Chem. Rev.* **2014**, *114*, 9662−9707.
(42) Archana, P.; Gupta, A.; Yusoff, M. M.; Jose, R. Tungsten doped titanium dioxide nanowires for high efficiency dye-sensitized solar cells. *Phys. Chem. Chem. Phys.* **2014**, *16*, 7448−7454.
(43) Weon, S.; Choi, W. TiO_2 nanotubes with open channels as deactivation-resistant photocatalyst for the degradation of volatile organic compounds. *Environ. Sci. Technol.* **2016**, *50*, 2556−2563.
(44) Dutta, S.; Patra, A. K.; De, S.; Bhaumik, A.; Saha, B. Self-assembled TiO_2 nanospheres by using a biopolymer as a template and its optoelectronic application. *ACS Appl. Mater. Interfaces* **2012**, *4*, 1560−1564.
(45) Mu, W.; Jia, Z.; Cittadino, G.; Yin, Y.; Luperini, C.; Hu, Q.; Li, Y.; Zhang, J.; Tonelli, M.; Tao, X. Ti-Doped β-Ga_2O_3: A Promising Material for Ultrafast and Tunable Lasers. *Cryst. Growth Des.* **2018**, *18*, 3037−3043.
(46) Zhu, T.; Gao, S.-P. The stability, electronic structure, and optical property of TiO2 polymorphs. *J. Phys. Chem. C* **2014**, *118*, 11385−11396.
(47) Yang, D.; Liu, H.; Zheng, Z.; Yuan, Y.; Zhao, J.-c.; Waclawik, E. R.; Ke, X.; Zhu, H. An efficient photocatalyst structure: TiO_2 (B) nanofibers with a shell of anatase nanocrystals. *J. Am. Chem. Soc.* **2009**, *131*, 17885−17893.
(48) Li, X.; Zhen, X.; Meng, S.; Xian, J.; Shao, Y.; Fu, X.; Li, D. Structuring β-Ga_2O_3 photonic crystal photocatalyst for efficient degradation of organic pollutants. *Environ. Sci. Technol.* **2013**, *47*, 9911−9917.
(49) Syed, N.; Zavabeti, A.; Mohiuddin, M.; Zhang, B.; Wang, Y.; Datta, R. S.; Atkin, P.; Carey, B. J.; Tan, C.; van Embden, J.; Chesman, A. S. R.; Ou, J. Z.; Daeneke, T.; Kalantar-zadeh, K. Sonication-Assisted Synthesis of Gallium Oxide Suspensions Featuring Trap State Absorption: Test of Photochemistry. *Adv. Funct. Mater.* **2017**, *27*, 1702295.
(50) Kresse, G.; Furthmüller, J. Efficient iterative schemes for ab initio total-energy calculations using a plane-wave basis set. *Phys. Rev. B: Condens. Matter Mater. Phys.* **1996**, *54*, 11169−11186.
(51) Blöchl, P. E. Projector augmented-wave method. *Phys. Rev. B: Condens. Matter Mater. Phys.* **1994**, *50*, 17953−17979.
(52) Peelaers, H.; Van de Walle, C. G. Brillouin zone and band structure of β-Ga_2O_3. *Phys. Status Solidi B* **2015**, *252*, 828−832.
(53) Heyd, J.; Scuseria, G. E.; Ernzerhof, M. Hybrid functionals based on a screened Coulomb potential. *J. Chem. Phys.* **2003**, *118*, 8207−8215.
(54) Peelaers, H.; Varley, J. B.; Speck, J. S.; Van de Walle, C. G. Structural and electronic properties of Ga2O3-Al2O3 alloys. *Appl. Phys. Lett.* **2018**, *112*, 242101.
(55) Mu, S.; Peelaers, H.; Van de Walle, C. G. Ab initio study of enhanced thermal conductivity in ordered AlGaO3 alloys. *Appl. Phys. Lett.* **2019**, *115*, 242103.
(56) Freysoldt, C.; Grabowski, B.; Hickel, T.; Neugebauer, J.; Kresse, G.; Janotti, A.; Van de Walle, C. G. First-principles calculations for point defects in solids. *Rev. Mod. Phys.* **2014**, *86*, 253−305.
(57) Juma, A. O.; Arbab, E. A.; Muiva, C. M.; Lepodise, L. M.; Mola, G. T. Synthesis and characterization of CuO-NiO-ZnO mixed metal oxide nanocomposite. *J. Alloys Compd.* **2017**, *723*, 866−872.
(58) Singh, D.; Mallesham, B.; Deshinge, A.; Joshi, K.; Ranjith, R.; Balakrishnan, V. Nanomechanical behavior of Pb $(Fe_{0.5-x}Sc_xNb_{0.5})O_3$ multiferroic ceramics. *Mater. Res. Express* **2018**, *5*, 116303.
(59) Peelaers, H.; Van de Walle, C. Doping of Ga_2O_3 with transition metals. *Phys. Rev. B: Condens. Matter Mater. Phys.* **2016**, *94*, 195203.
(60) Dillon, S. J.; Harmer, M. P. In *Diffusion controlled abnormal grain growth in ceramics*. *Mater. Sci. Forum* **2007**, *558-559*, 1227−1236.
(61) Gülgün, M. A.; Voytovych, R.; Maclaren, I.; Rühle, M.; Cannon, R. M. Cation segregation in an oxide ceramic with low solubility: yttrium doped α-alumina. *Interface Sci.* **2002**, *10*, 99−110.
(62) Wang, C. M.; Chan, H. M.; Harmer, M. P. Effect of Nd2O3 Doping on the Densification and Abnormal Grain Growth Behavior of High-Purity Alumina. *J. Am. Ceram. Soc.* **2004**, *87*, 378−383.
(63) Jung, Y. I.; Lee, B. K.; Kang, S. J. L. Effect of $Ba_6Ti_{17}O_{40}$/$BaTiO_3$ interface structure on {111} twin formation and abnormal grain growth in $BaTiO_3$. *J. Am. Ceram. Soc.* **2004**, *87*, 739−741.
(64) Rubio, E.; Mates, T.; Manandhar, S.; Nandasiri, M.; Shutthanandan, V.; Ramana, C. V. Tungsten incorporation into gallium oxide: Crystal structure, surface and interface chemistry, thermal stability, and interdiffusion. *J. Phys. Chem. C* **2016**, *120*, 26720−26735.
(65) Ramana, C. V.; Rubio, E.; Barraza, C.; Miranda Gallardo, A.; McPeak, S.; Kotru, S.; Grant, J. Chemical bonding, optical constants, and electrical resistivity of sputter-deposited gallium oxide thin films. *J. Appl. Phys.* **2014**, *115*, 043508.
(66) Lopez, I.; Utrilla, A. D.; Nogales, E.; Mendez, B.; Piqueras, J.; Peche, A.; Ramírez-Castellanos, J.; González-Calbet, J. M. In-doped gallium oxide micro-and nanostructures: morphology, structure, and luminescence properties. *J. Phys. Chem. C* **2012**, *116*, 3935−3943.
(67) Patil, S. B.; Kim, I. Y.; Gunjakar, J. L.; Oh, S. M.; Eom, T.; Kim, H.; Hwang, S.-J. Phase tuning of nanostructured gallium oxide via hybridization with reduced graphene oxide for superior anode performance in Li-ion battery: an experimental and theoretical study. *ACS Appl. Mater. Interfaces* **2015**, *7*, 18679−18688.
(68) Wang, E.; Yang, W.; Cao, Y. Unique surface chemical species on indium doped TiO_2 and their effect on the visible light photocatalytic activity. *J. Phys. Chem. C* **2009**, *113*, 20912−20917.
(69) Tauc, J.; Grigorovici, R.; Vancu, A. Optical properties and electronic structure of amorphous germanium. *Phys. Status Solidi B* **1966**, *15*, 627−637.
(70) Tauc, J. Optical properties and electronic structure of amorphous Ge and Si. *Mater. Res. Bull.* **1968**, *3*, 37−46.
(71) Chung, Y.; Lo, W.; Somorjai, G. Low energy electron diffraction and electron spectroscopy studies of the clean (110) and

https://dx.doi.org/10.1021/acs.cgd.9b00747
Cryst. Growth Des. 2020, 20, 1422−1433

(100) titanium dioxide (rutile) crystal surfaces. *Surf. Sci.* **1977**, *64*, 588−602.
(72) Zhao, X.; Feng, J.; Wang, N.; Yao, X.; Chen, W.; Chen, S.; Huang, Z.; Chen, Z. The Influence of Ti Doping on Morphology and Photoelectrochemical Properties of Hematite Grown from Aqueous Solution for Water Splitting. *Energy Technology* **2018**, *6*, 2188−2199.
(73) Thomas, N.; Nobe, K. Kinetics of the hydrogen evolution reaction on titanium. *J. Electrochem. Soc.* **1970**, *117*, 622−626.

https://dx.doi.org/10.1021/acs.cgd.9b00747
Cryst. Growth Des. 2020, 20, 1422−1433